

Thermally adaptive textile inspired by morpho butterfly for all-season comfort and visible aesthetics

Zhuowen Xie^{1#}, Yan Wang^{1#}, Ting-Ting Li¹, Wangkai Jiang^{1*}, Honglei Cai¹, Jun Zhang¹, Hui Wang¹, Jianchen Hu^{1*}, Ke-Qin Zhang^{1*}

1 National Engineering Laboratory for Modern Silk, College of Textile and Clothing Engineering, Soochow University, Suzhou, Jiangsu 215123, China

ABSTRACT

A longstanding challenge in personal thermal management has been transitioning from static, appearance-limited passive radiative cooling (PDRC) materials to systems that are both dynamically adaptive and visually versatile. The central hurdle remains the inherent compromise between color saturation and cooling power. Inspired by organisms such as butterflies, which decouple structural color from thermal function, we present a smart textile that seamlessly merges a dynamic thermochromic layer with static photonic crystals (PCs). This design enables the solar reflectance to be autonomously switched—from approximately 0.6 in the colored state for heating to about 0.9 in the high-reflectance state for cooling. Consequently, outdoor experiments validated substantial temperature regulation: the fabric achieves a surface temperature reduction of 3–4 °C in summer and a heating difference of <1 °C in winter compared to commercial reference materials, all while maintaining high-saturation colors. This dual-mode operation offers a viable pathway for achieving adaptive, aesthetic, and energy-free thermal comfort.

1 Introduction

The pursuit of energy-efficient personal thermal management (PTM)¹⁻³ is crucial amid growing global energy demands, driven significantly by the need to manage the vast and spectrally diverse solar energy⁴⁻⁶ incident on Earth (Fig. 1a). Passive daytime radiative cooling (PDRC) materials⁷⁻⁹, leveraging the atmospheric transparency window (8–13 μm) for heat dissipation and reflecting a substantial portion of incident solar radiation, offer a key zero-energy cooling solution. However, a critical bottleneck emerges when integrating vibrant color: since visible (VIS) light constitutes nearly half of the solar energy spectrum (Fig. 1b), high-saturation colors often rely on absorption in this region, thereby diminishing the material's solar reflectance and counteracting its cooling potential¹⁰. This inherent trade-off, coupled with the predominantly static nature of current colored PDRC materials, limits their adaptive capacity and broader applicability.

To overcome these limitations and achieve dynamic thermal regulation, a fundamental shift towards actively managing solar absorption across the VIS spectrum is necessary.¹¹⁻¹⁴ We propose a conceptual framework centered on a dynamic optical switch (Fig. 1c), wherein a material toggles between a high-reflectance state for cooling under intense solar irradiation and a controlled absorption state to harness thermal energy when needed. Theoretical modeling based on this principle (Fig. 1d and Fig. S1) indicates that such bidirectional regulation of VIS light can yield substantial modulation of radiative heat transfer, enabling significant cooling and heating capabilities solely through VIS spectrum management. For example, Qu et al.¹⁵ fabricated a textile functionalized with thermochromic microcapsules (TCMs)—encapsulated in graphene and barium sulfate coatings—that adapted to ambient temperature (T_{amb}) fluctuations, shifting color between black and white. This textile demonstrated maximized temperature regulation by exploiting optical changes. However, such approaches often face challenges in decoupling color from thermal management, limiting color diversity.

This concept finds compelling precedence in nature: studies have shown that structurally identical coloration on different substrates (black or white) alters thermal equilibrium under sunlight¹⁶⁻¹⁸—a phenomenon we explored in morpho butterflies'

wings under simulated solar irradiation. Our results reveal that structurally identical blue coloration atop black versus white substrates results in markedly different equilibrium temperatures, directly attributed to differential solar heat absorption by the underlying layer (Fig. 1e and Fig. S2). This natural phenomenon underscores the potential to decouple visual appearance from thermal performance. To achieve this decoupling, a distinct architectural design is essential. By isolating the color-producing function from the thermal-responsive function, independent control of visual appearance and thermal properties becomes feasible.

Inspired by this bio-insight, we engineered a colorful smart adaptive (CSA) fabric featuring a thermally responsive optical architecture. As schematically depicted in Fig. 1f, our design integrates a thermochromic nanofiber membrane—capable of reversibly switching its optical properties (effectively altering solar absorption) between a reflective white state and an absorptive dark state—with a structurally colored photonic crystals (PCs) layer. The PCs layer provides stable, high-saturation color independent of the underlying thermal state, while the nanofiber matrix ensures high mid-infrared emissivity (ε_{MIR}) (Fig. S3). This synergistic combination allows the textile to autonomously regulate its energy exchange with the environment: maintaining high solar reflectance ($\rho_{solar} \approx 0.9$) and cooling in high thermal load conditions, and enhancing solar absorption ($\alpha_{solar} \approx 0.4-0.5$) for passive heating when needed. Notably, it achieves a maximum cooling effect of up to 3–4 °C under high temperatures and a heating difference of <1 °C under low temperatures compared to commercial reference materials. Furthermore, it allows for the recoloring of thermal management textiles, promising to meet varied aesthetic demands that are often sacrificed in traditional designs. Such decoupled structures can facilitate easy color customization without compromising cooling or heating efficiency, addressing the long-standing issue of color-thermal integration.

Results

2.1 Characterization and optical properties of SA fabric

To realize intelligent temperature regulation, we fabricated smart adaptive (SA)

fabric *via* electrospinning poly(vinylidene fluoride-co-hexafluoropropylene) (PVDF-HFP) nanofiber membranes embedded with thermochromic microcapsules (TCMs) (Fig. S4). The incorporated TCMs enable reversible switching of the membrane's optical appearance between a black (heating state) and a white (cooling state)¹⁴, manifesting as a white appearance in cooling mode and black in heating mode. Scanning electron microscopy (SEM) imaging (Fig. 2a) reveals a randomly interwoven fiber network with TCMs uniformly distributed on fiber surfaces. To optimize radiative cooling, the fiber diameter distribution was statistically analyzed based on Mie scattering theory^{19,20}, as diameter critically governs scattering behavior and thus solar reflectance. Further analysis *via* MATLAB²¹-calculated scattering efficiency (Q_{sca}) versus fiber diameter (Fig. 2c) reveals that the broad fiber diameter distribution (0.3–1.3 μm) of the electrospun membrane exhibits significant scattering efficiency across the solar spectrum (0.3–2.5 μm). Specifically, fibers with diameters >680 nm efficiently scatter near-infrared (NIR, 0.75–2.5 μm) light, while those <680 nm contribute to VIS light (0.4–0.75 μm) scattering. Consequently, the SA fabric maintains high NIR reflectance (providing a baseline for cooling mode) and enhanced total solar reflectance in the cooling state, where TCMs do not absorb VIS light.

The mechanism (Fig. 2d) of reversible thermochromism relies on TCMs composed of a color former (incorporating lactone and fluorescein dyes), a color developer, and a solvent²². At lower temperatures (<25 °C, heating state), interaction between the color former and developer induces lactone ring-opening, forming an extended conjugated system that absorbs VIS light (black state). At elevated temperatures (>30 °C, cooling state), the color former undergoes molecular rearrangement (not merely electron gain) leading to lactone ring closure, disrupting the conjugated structure. This transition shifts the TCMs from broadband VIS absorption (black) to high reflectance (white), as confirmed by macroscopic optical changes. Notably, thickness optimization (Fig. S5) revealed that a thickness of 0.45 mm maximizes the difference in solar reflectance between cooling and heating modes.

Additionally, Fourier transform infrared (FTIR) spectroscopy (Fig. S6) confirms that the SA fabric exhibits abundant absorption peaks in the atmospheric transparency

window, with high ε_{MIR} (≈ 0.94 , Fig. 2e) maintained in both states. This combination of switchable solar reflectance and constant high thermal emissivity underpins bidirectional thermal management. To demonstrate intuitive thermal visualization, the SA fabric was placed on adjacent temperature-controlled plates set to 15 °C (low-temperature end) and 35 °C (high-temperature end), exhibiting a clear visual temperature difference (Fig. S7). The full spectral response of the fabric is summarized in Fig. 2e, validating its dual-mode optical regulation.

The reversible optical switching of the SA fabric exhibits excellent robustness. Cyclic VIS reflectance measurements (Fig. 2f and Fig. S8) show minimal degradation was observed after 10 thermally induced switching cycles (15–35 °C), confirming stability essential for practical applications. To validate the temperature-adaptive thermal management of the SA fabric, we conducted indoor simulated sunlight experiments (Fig. 2g) using a solar simulator (0–1000 W m⁻², AM 1.5G filter) under controlled conditions ($T_{amb}=10$ °C, no forced convection), with samples including SA fabric, commercial black cotton (traditional absorber), and white PDRC reference (pristine PVDF-HFP electrospun membrane). As light intensity increased gradually, the SA fabric (Fig. 2h) initially operated in a heating state: below 25 °C (TCMs in absorptive black state, no VIS color change), its temperature evolution mirrored commercial black cotton, exhibiting a similar rapid heating rate. At ~ 400 W m⁻², the SA fabric's temperature surpassed 25 °C, triggering TCMs to switch to a reflective white state (cooling mode). Thereafter, even as light intensity further increased to 1000 W m⁻², its heating rate decelerated significantly, stabilizing at ~ 28 °C. In contrast, commercial black cotton continued heating to a steady-state temperature of ~ 45 °C at 1000 W m⁻², while the white PDRC reference maintained a consistently low temperature (~ 18 °C) across all intensities. These results confirm the SA fabric's autonomous regulation: it mimics black cotton for efficient passive heating at low temperatures (< 25 °C) and switches to white-like cooling at high temperatures (> 25 °C), limiting temperature rise to ~ 28 °C even under intense sunlight, thereby demonstrating robust temperature-adaptive thermal management.

2.2 Optical-thermal performance of CSA fabric

To achieve multi-color integration in thermal management textiles while decoupling aesthetics from functionality, we engineered a colorful smart adaptive (CSA) fabric by integrating colloidal PCs onto the surface of the previously developed SA fabric through a spraying process (Fig. 3a). This layered architecture combines the SA fabric's thermochromic switching (heating/cooling states) with the PCs' angle-independent structural color, enabling customizable coloration without compromising thermal regulation. The CSA fabric features a hierarchical structure: a bottom layer of the SA fabric (PVDF-HFP nanofiber membrane embedded with TCMs) for reversible solar absorption/reflection, and a top layer of colloidal PCs deposited by spray-coating after synthesis by emulsion polymerization (details in Figs. S9–S13). SEM image of the CSA fabric's cross-section (Fig. 3b) reveals a top surface of randomly assembled PCs (non-crystalline arrangement, high-magnification insets) and an internal nanofiber matrix with uniformly distributed TCMs. The confined assembly of PCs on the nanofiber surface minimizes structural defects, endowing the fabric with high-brightness, saturated structural colors.

The structural color of the CSA fabric originates from Bragg diffraction by the PC monolayer, governed by the Bragg-Snell law^{23,24}:

$$\lambda_{Bragg} = \frac{2\sqrt{6}}{3} d (n_{eff}^2 - \sin^2 \theta)^{\frac{1}{2}} \quad (1)$$

where λ_{Bragg} is the wavelength of reflected light, d is the diameter of colloidal nanoparticles, n_{eff} is the effective refractive index of the periodic structure, and θ is the incident angle of light relative to the normal. By adjusting d , the reflected wavelength (and thus color) can be tuned across the VIS spectrum. For example, PCs with diameters of 190 nm, 220 nm, and 240 nm can produce blue, green, and red structural colors, respectively (reflection spectra in Fig. S11). These colors are non-iridescent (angle-independent, Fig. S13), as confirmed by consistent chromaticity coordinates on the CIE 1931 diagram (Fig. 3c), making them suitable for aesthetic applications requiring stable coloration.

The thermal regulation of the CSA fabric hinges on the reversible switching of ρ_{solar} between two modes: passive heating, where TCMs adopt an absorptive state, and radiative cooling, where TCMs switch to a reflective state. As illustrated in Fig. 3d, three representative CSA fabrics (red, green, and blue) exhibit distinct optical behaviors. In the heating state (solid lines), all fabrics display low ρ_{solar} (≈ 0.5 – 0.6 , particularly in the VIS region), dominated by TCM absorption to facilitate passive heating. Crucially, each color variant retains a Bragg peak characteristic of structural color (from PCs) in both heating and cooling states, confirming the stability of the color-generating mechanism independent of thermal switching. In the cooling state (dashed lines), ρ_{solar} rises sharply to ≈ 0.8 – 0.9 , attributed to the white state of the substrate SA fabric and enhanced reflection from the PCs layer. The reflectance difference between states exceeds 30% across the solar spectrum (0.3–2.5 μm), enabling efficient bidirectional thermal control. Notably, the integration of the PCs-based structural color layer does not compromise the SA fabric's infrared emissivity. Taking the green CSA fabric as an example (Fig. S14), MIR emissivity analysis reveals a high $\varepsilon_{MIR} \approx 0.94$ within the atmospheric transparency window in both heating and cooling modes. This consistency holds for all structural colors, indicating the PCs layer minimally interferes with the thermal radiation properties of the underlying substrate. Cyclic stability tests (20 thermally induced switching cycles between 15–35 °C, Fig. 3e and Fig. S15) further validate long-term reliability, confirming that the PCs-integrated structure retains thermal performance of CSA fabric over repeated use.

To demonstrate practical applicability, Fig. 3f shows a flower-patterned CSA fabric (spray-coated with red, green, and blue structural colors onto the substrate SA fabric, Fig. S16) under simulated sunlight at two T_{amb} : cool (20 °C) and hot (35 °C). The patterned regions exhibit clear color transitions: at 35 °C, the colors fade gradually due to TCM switching to the reflective state, while at 20 °C, vibrant hues reappear as TCMs absorb light. Temperature mapping reveals that the colored regions (with black TCMs) achieve higher temperatures than the ambient environment under heating mode, whereas uncolored areas remain relatively cooler. Critically, selective adjustment of the TCMs' phase transition temperature can precisely tune the transition interval between

cooling and heating states and enable the fabric to exhibit corresponding colors (Fig. S17). This visual-thermal correlation underscores the fabric's ability to dynamically balance aesthetic expression and thermal function in real-world scenarios.

2.3 Outdoor evaluation of dual-mode CSA fabric

To validate the autonomous thermal regulation of the CSA fabric under real-world conditions, outdoor experiments were conducted in Suzhou, Jiangsu Province (31.3° N, 120.7° E), over three hours under low- ($\approx 15^{\circ}$ C) and high- ($\approx 35^{\circ}$ C) temperature regimes. Photographic documentation of the samples (Fig. 4a) revealed clear temperature-dependent color transitions: at high temperatures ($\approx 35^{\circ}$ C), all CSA fabrics—regardless of initial structural color (blue, green, red, or black)—switched to a white state due to TCM activation, while at low temperatures ($\approx 15^{\circ}$ C), they retained vivid structural colors, confirming the stability of the PCs-based structural coloration mechanism.

The experimental setup (Fig. 4b and Fig. 4c) was designed based on classic PDRC measurement platform^{25,26} to minimize parasitic heat exchange. It consisted of a thermally insulated chamber housing three circular CSA fabric samples (diameter: 90 mm). The chamber featured an aluminum foil-coated foam enclosure (to reflect external radiation and reduce conductive heat loss), a foam-insulated sample stage (to isolate samples from ground heat), and copper thermal contact sheets (to ensure uniform heat transfer between samples and temperature sensors). A temperature monitoring system recorded real-time sample temperatures, while a pyranometer and thermocouples tracked solar irradiance and ambient conditions, respectively. This configuration enabled precise quantification of the fabric's thermal response under natural sunlight.

Under high-temperature conditions (humidity and wind speed were recorded in Fig. S18a), Fig. 4d (left panel) showed that the surface temperatures of the CSA fabrics were consistently 3–4 °C (Fig. S19a) lower than those of corresponding commercial-colored fabrics. This cooling effect is attributed to the CSA fabrics' transition to a reflective state, where TCMs switch to a white morphology, achieving high solar reflectance ($\rho_{solar} \approx 0.8\text{--}0.9$) and stable mid-infrared emission ($\varepsilon_{MIR} \approx 0.94$) for radiative heat dissipation. At low temperatures (humidity and wind speed were recorded in Fig.

S18b), the CSA fabrics retained their structural color (photographic evidence in Fig. 4a), with low solar absorptance ($\alpha_{solar} \approx 0.4-0.5$) comparable to commercial colorful fabrics (Fig. 4b, right panel). The temperature difference between the CSA fabrics and commercial counterparts was negligible (<1 °C, Fig. S19b), indicating that the TCMs in the absorptive state minimized performance gaps. This enables effective passive heating through solar energy capture, while the stable structural coloration (from PCs) preserves aesthetic appeal—a key advantage over conventional heating textiles that sacrifice color for functionality. Notably, the SA fabric without the structural color coating also exhibited similar thermal management performance (Figs. S20-S21), with comparable temperature regulation and radiative properties (ρ_{solar} and ε_{MIR}). This confirms that the thermal regulation function of the CSA fabric is largely decoupled from the structural color, underscoring that the core thermochromic switching (*via* TCMs) drives bidirectional thermal management, while the PC layer solely contributes to aesthetics.

Theoretical calculations based on radiative heat transfer models^{27,28} (Fig. 4e) systematically quantified the cooling and heating power of CSA fabrics with distinct structural colors (red, green, and blue) under varying non-radiative heat exchange coefficients ($h = 0, 3, 6, 9, 12$ W m⁻² K⁻¹), which represent different environmental convection conditions (from cool to hot). At cool environment ($T_{amb}=15$ °C), the CSA fabrics achieved a net heating power of ~ 300 W m⁻², accounting for solar absorption, thermal emission, and convective losses. At hot environment ($T_{amb}=35$ °C), they delivered a net cooling power of $\sim 50-60$ W m⁻². This switchable power profile—governed by the TCMs' phase transition temperature—validates the CSA fabrics' autonomous transition from solar heating (low temperature) to radiative cooling (high temperature), with performance robustness across diverse climatic convection conditions.

To evaluate the energy-saving potential of the CSA fabric in practical building applications, we used EnergyPlus^{29,30} to generate annual energy-saving maps for apartment buildings (Fig. S22a), comparing CSA fabrics (red, green, blue structural colors) with commercial colored textiles. The analysis focused on dual-mode thermal

regulation (heating/cooling) under real-world climatic conditions. As shown in the energy-saving maps (Fig. 4f (details in Fig. S22b)), CSA fabrics of all colors demonstrated superior performance to commercial counterparts, with energy savings consistently exceeding $5\text{--}15\text{ MJ m}^{-2}$ across diverse climate zones (especially green CSA fabric). Notably, in Guangzhou (southern China, subtropical climate), the CSA fabrics achieved an exceptional energy saving of $\sim 40\text{ MJ m}^{-2}$ —significantly higher than commercial textiles. This advantage arises because commercial colored fabrics, with fixed solar absorptance, fail to meet cooling demands in high-temperature southern regions, leading to excessive HVAC loads. In contrast, the CSA fabrics autonomously switch to a reflective white state ($T_{amb} > 25\text{ }^{\circ}\text{C}$) under intense sunlight, enhancing radiative cooling and reducing HVAC energy consumption compared to static commercial fabrics. Collectively, the CSA fabrics enable efficient dual-mode thermal management (cooling/heating) with color-agnostic performance and practical energy-saving potential.

2.4 Application performance and multifunctional advantages of CSA fabric

A key demonstration of this design is the CSA fabric's color-rewritable behavior. A CSA fabric sample printed with a blue “Soochow” pattern underwent simple washing (deionized water, $40\text{ }^{\circ}\text{C}$, 30 min) and drying ($60\text{ }^{\circ}\text{C}$, 2 h), which effectively removed the original blue pattern. Subsequent spraying of a green “Zhang Group” pattern onto the cleaned surface transformed the fabric into a green-structured variant (Fig. 5b). Spectral analysis (Fig. S23) confirmed that the rewritten pattern retained optical properties (ρ_{solar}) nearly identical to the original pattern of the same color series. This rewrability arises from the physical self-assembly of PCs on the SA fabric surface, enabling reversible detachment/reattachment of the PCs layer—an advantage unachievable with traditional dye-based coloration.

Beyond thermal and optical functions, the CSA fabric exhibits exceptional physicochemical properties derived from its PVDF-HFP matrix. The high fluorine content (C-F bonds)³¹ endows it with superhydrophobicity, evidenced by a water contact angle (WCA) of $138^{\circ}\pm 2^{\circ}$ (Fig. 5c). Combined with its nanofiber structure, this

property grants excellent waterproofing and air permeability (Fig. 5d), critical for wearable comfort. These attributes position the fabric as a promising candidate for personal thermal management.

To comprehensively evaluate the potential of the CSA fabric for thermal management textiles, we summarized and compared its performance with existing radiation modulating materials^{13-15,32} in terms of functional decoupling, color versatility, thermal efficiency, wearability, and multifunctionality *via* a Radar plot in Fig. 5e. The CSA fabric's modular architecture—enabling independent control of structural color, dynamic thermal switching, NIR reflection, and MIR emissivity—resolves the color-thermal trade-off, achieves full VIS spectrum coverage (surpassing limited hues of prior work), delivers a 30–40% higher solar reflectance contrast (outperforming static/single-mode textiles), and integrates superhydrophobicity with breathability for wearability. Unique color rewritability further adds multifunctionality. This comprehensive superiority showcases its potential as next-generation thermal management textiles.

Real-world utility was validated through two prototypes. A wearable smart thermal management textile (flower-patterned CSA fabric laminated onto a dark gray garment, Fig. 5f) exhibited reversible color switching—white at high temperatures and retaining structural color at low temperatures. In a climate chamber (400 W m⁻² simulated sunlight), its surface temperature rose to 35°C at 12°C ambient (approaching the garment's temperature) and dropped to 25°C at 32°C ambient (significantly lower than the garment), with thermal imaging (Fig. 5f inset) confirming localized heating/cooling. An intelligent tent (20×10×10 cm³, Fig. 5g) fabricated from CSA fabric maintained a stable internal microenvironment: at hot environment, the white state CSA fabric reflected solar radiation and dissipated heat *via* the atmospheric window; at cold environment, the colored state (TCMs absorptive) absorbed solar energy while retaining hue, raising internal temperature. These prototypes underscore the fabric's adaptability for wearable and outdoor thermal management, leveraging autonomous color switching and dual-mode regulation.

3 Conclusion

In summary, we introduce a CSA fabric that resolves the inherent conflict between aesthetic coloration and thermal management in personal thermal regulation. By decoupling structural color, dynamic thermal switching, and radiative properties through a modular architecture, we engineered a textile capable of autonomous bidirectional thermal regulation—radiative cooling under high temperatures and passive heating under low temperatures—while maintaining stable, customizable structural colors. This design breaks the limitation of traditional colored thermochromic materials, where color and thermal performance are entangled, enabling color-agnostic thermal management across the VIS spectrum. The CSA fabric demonstrates remarkable versatility through its color-rewritable capability (pattern transformation *via* simple washing), exceptional physicochemical properties for wearability, and proven utility in wearable textiles and intelligent tents. Energy simulations highlight its potential to reduce building HVAC energy consumption, underscoring its value for sustainable thermal management. By merging aesthetic freedom with adaptive thermal intelligence, this work offers a concrete path to dynamic textiles for personalized apparel and energy-smart architecture.

References

- 1 Wu, R. *et al.* Spectrally engineered textile for radiative cooling against urban heat islands. *Science* **384**, 1203-1212 (2024).
- 2 Wu, X. *et al.* An all-weather radiative human body cooling textile. *Nature Sustainability* **6**, 1446-1454 (2023).
- 3 Liu, J., Du, Y., Zhang, S. & Yan, J. Spectrally engineered textiles for personal cooling. *Joule* **8**, 2727-2731 (2024).
- 4 Wang, Z. *et al.* Self-sustaining personal all-day thermoregulatory clothing using only sunlight. *Science* **382**, 1291-1296 (2023).
- 5 Liu, J.-Z. *et al.* Large-area radiation-modulated thermoelectric fabrics for high-performance thermal management and electricity generation. *Science Advances* **11**, eadr2158 (2025).
- 6 Fick, S. E. & Hijmans, R. J. WorldClim 2: new 1-km spatial resolution climate surfaces for global land areas. *International journal of climatology* **37**, 4302-4315 (2017).
- 7 Li, J. *et al.* A photosynthetically active radiative cooling film. *Nature Sustainability* **7**, 786-795 (2024).
- 8 Fu, Y. *et al.* Photoluminescent radiative cooling for aesthetic and urban comfort. *Nature Sustainability*, 1-12 (2025).
- 9 Yang, K. *et al.* Towards practical applications of radiative cooling. *Nature Reviews Clean Technology*, 1-20 (2025).
- 10 Wang, T. *et al.* Colored radiative cooling: from photonic approaches to fluorescent colors and beyond. *Advanced Materials* **37**, 2414300 (2025).
- 11 Saju, S. K. *et al.* Thermochromic polymer blends. *Joule* **8**, 2696-2714 (2024).
- 12 Zhang, Q., Wang, Y., Lv, Y., Yu, S. & Ma, R. Bioinspired zero-energy thermal-management device based on visible and infrared thermochromism for all-season energy saving. *Proceedings of the National Academy of Sciences* **119**, e2207353119 (2022).
- 13 Zhou, P., Jiang, G., Wang, Y., Tian, Y. & Zhang, X. Self-adaptive and large-area sprayable thermal management coatings for energy saving. *Nature Communications* **16**, 3791 (2025).
- 14 Liu, B. Y. *et al.* Bioinspired superhydrophobic all-in-one coating for adaptive thermoregulation. *Advanced Materials* **36**, 2400745 (2024).
- 15 Zhu, K. *et al.* Temperature-adaptive dual-modal photonic textiles for thermal management. *Science Advances* **10**, eadr2062 (2024).
- 16 Cao, X. *et al.* Replicating the Cynandra opis butterfly's structural color for bioinspired bigrating color filters. *Advanced Materials* **34**, 2109161 (2022).
- 17 Butt, H. *et al.* Morpho butterfly-inspired nanostructures. *Advanced Optical Materials* **4**, 497-504 (2016).
- 18 Iwata, M., Teshima, M., Seki, T., Yoshioka, S. & Takeoka, Y. Bio-inspired bright structurally colored colloidal amorphous array enhanced by controlling thickness and black background. *Advanced Materials* **29**, 1605050 (2017).
- 19 Jiang, W. *et al.* Scalable self-cooling textile enabled by hierarchical nanofiber structures with thermoelectric properties. *Device* **3**, 100564 (2025).
- 20 Liu, R. *et al.* Materials in radiative cooling technologies. *Advanced Materials* **37**, 2401577 (2025).
- 21 Chen, D.-C. *et al.* Superdurable, Flexible ceramic nanofibers for sustainable passive radiative cooling. *ACS Nano* **19**, 28280-28294 (2025).

22 Xie, L. *et al.* “Change according to the situation”—Color-accommodative nature-skin-derived thermochromic membrane for active all-season thermal management. *Advanced Functional Materials* **34**, 2405582 (2024).

23 Li, Q. *et al.* Additive mixing and conformal coating of noniridescent structural colors with robust mechanical properties fabricated by atomization deposition. *ACS Nano* **12**, 3095-3102 (2018).

24 Hou, X. *et al.* Brilliant colorful daytime radiative cooling coating mimicking scarab beetle. *Matter* **8** (2025).

25 Wang, Z., Pian, S. & Ma, Y. Characterization of radiative cooling materials. *Nature Protocols*, 1-39 (2025).

26 Zhou, L., Yin, X. & Gan, Q. Best practices for radiative cooling. *Nature Sustainability* **6**, 1030-1032 (2023).

27 Fan, S. & Li, W. Photonics and thermodynamics concepts in radiative cooling. *Nature Photonics* **16**, 182-190 (2022).

28 Jiang, W. *et al.* Wearable passive thermal management functional textiles: Recent advances in personal comfort and energy harvesting applications. *Advanced Fiber Materials*, 1-41 (2025).

29 Lu, G. *et al.* Scalable metasurface-enhanced supercool cement. *Science Advances* **11**, eadv2820 (2025).

30 Ma, J.-W. *et al.* A photoluminescent hydrogen-bonded biomass aerogel for sustainable radiative cooling. *Science* **385**, 68-74 (2024).

31 Ganesh, V. A. *et al.* Superhydrophobic fluorinated POSS–PVDF-HFP nanocomposite coating on glass by electrospinning. *Journal of Materials Chemistry* **22**, 18479-18485 (2012).

32 Chen, Z. *et al.* An infrared-transparent textile with high drawing processed Nylon 6 nanofibers. *Nature Communications* **16**, 2009 (2025).

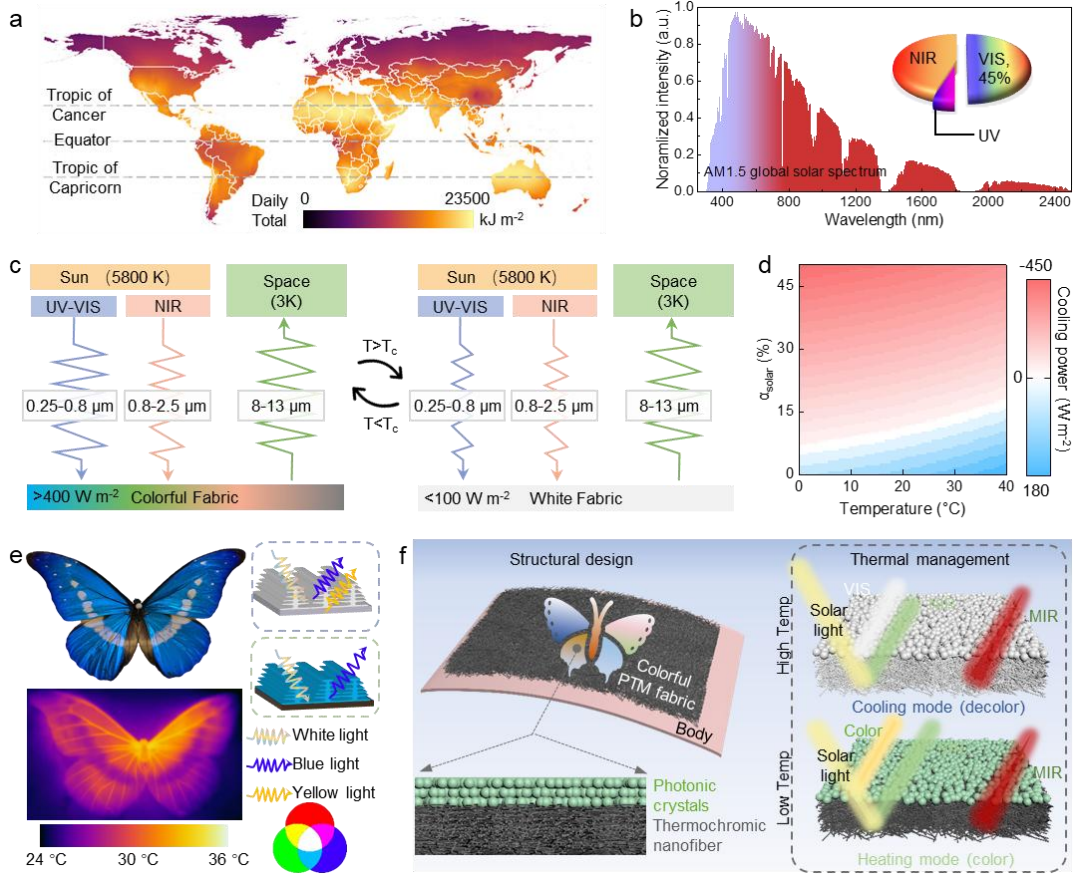


Fig. 1 Design of SA fabric and conceptual framework. a) Global spatial distribution of solar radiation. b) Spectral characteristics of the AM1.5 global solar spectrum. c) Switching mechanism of optical and thermal radiation properties in thermochromic passive daytime radiative cooling (PDRC) materials at different temperatures. d) Theoretical simulations of the relationship between solar absorbance and thermal power (positive: cooling power; negative: heating power). e) Digital and infrared photographs of a butterfly wing under simulated solar irradiation (600 W m^{-2}). f) Structural design and thermal management mechanism of the colorful smart adaptive (CSA) fabric.

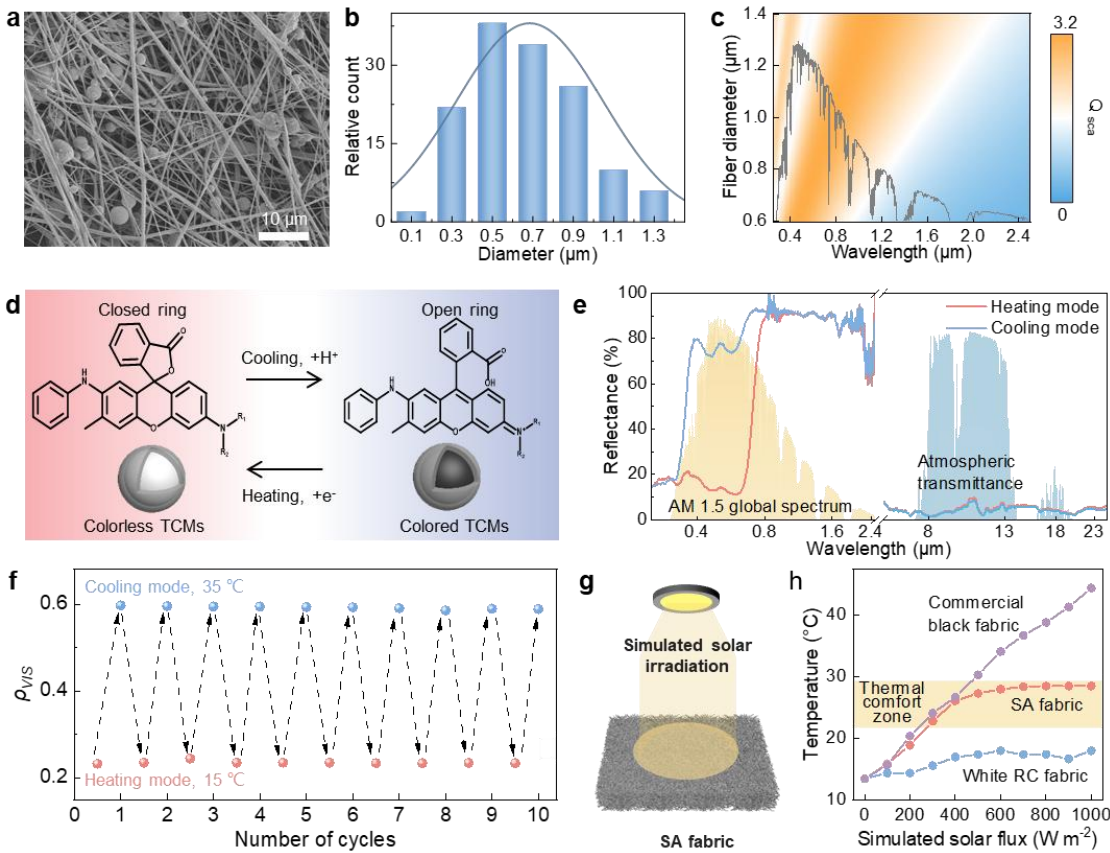


Fig. 2 Characterization and optical-thermal properties of SA fabric. a) SEM image of the electrospun PVDF-HFP nanofiber membrane with TCMs. b) Statistical distribution of fiber diameters. c) MATLAB-calculated Q_{sca} versus fiber diameter based on Mie scattering theory. d) Mechanism of reversible thermochromism in TCMs (color former, developer, solvent). e) Full spectral response of the SA fabric. f) Cyclic stability of VIS reflectance after 10 thermally induced switching cycles (15–35 °C). g) Indoor simulated sunlight experiment setup. h) Temperature evolution of SA fabric, commercial black cotton, and white PDRC reference under increasing light intensity (0–1000 W·m⁻²).

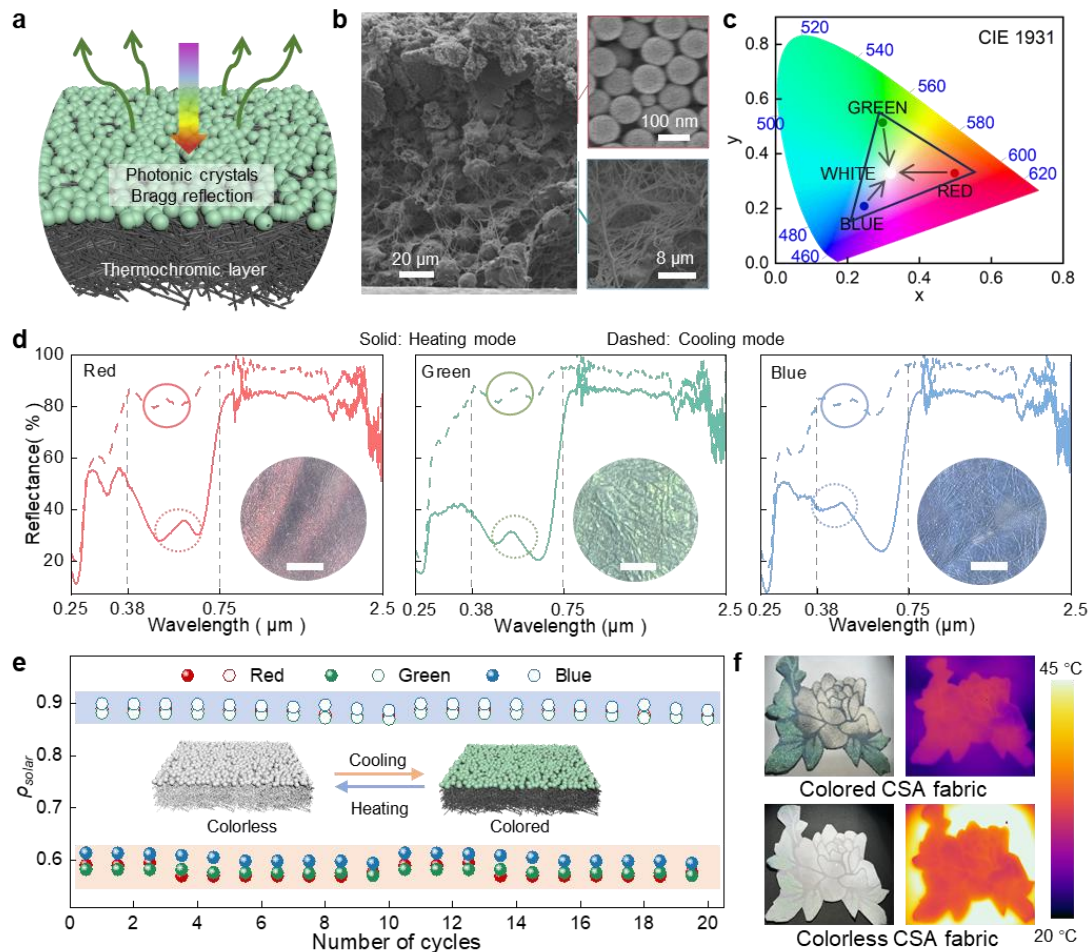


Fig. 3 Optical-thermal performance of CSA fabric. a) Schematic of CSA fabric fabrication via spraying colloidal PCs onto SA fabric. b) Cross-sectional SEM image of CSA fabric (top: PCs; bottom: nanofiber matrix with TCMs). c) CIE 1931 chromaticity diagram confirming non-iridescent structural colors. d) Spectra of red, green, and blue CSA fabrics in heating (solid) and cooling (dashed) states (Scale bar: 2 cm). e) Cyclic stability of thermal performance after 20 switching cycles (15–35 °C). f) Photo and thermal image of flower-patterned CSA fabric under simulated sunlight (20 °C and 35 °C).

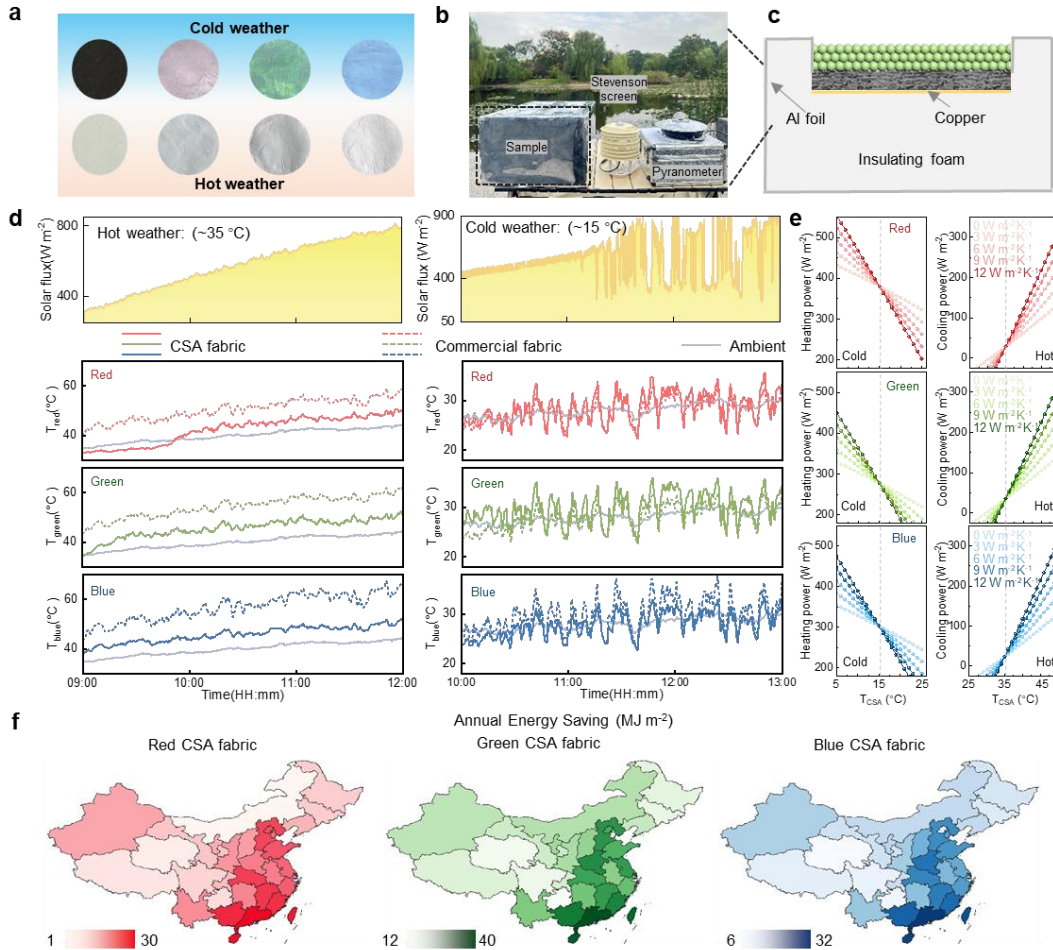


Fig. 4 Outdoor evaluation of dual-mode CSA fabric. a) Photographic documentation of CSA fabrics under low (~15 °C) and high (~35 °C) temperature regimes. b-c) Experimental setup for outdoor thermal regulation tests. d) Outdoor temperature comparison between CSA fabrics and commercial-colored fabrics (left: high temp; right: low temp). e) Theoretical calculations of cooling/heating power under varying convection conditions ($h= 0\text{--}12 \text{ W}\cdot\text{m}^{-2}\cdot\text{K}^{-1}$). f) Annual energy-saving maps (China mainland) comparing CSA fabrics with commercial textiles.

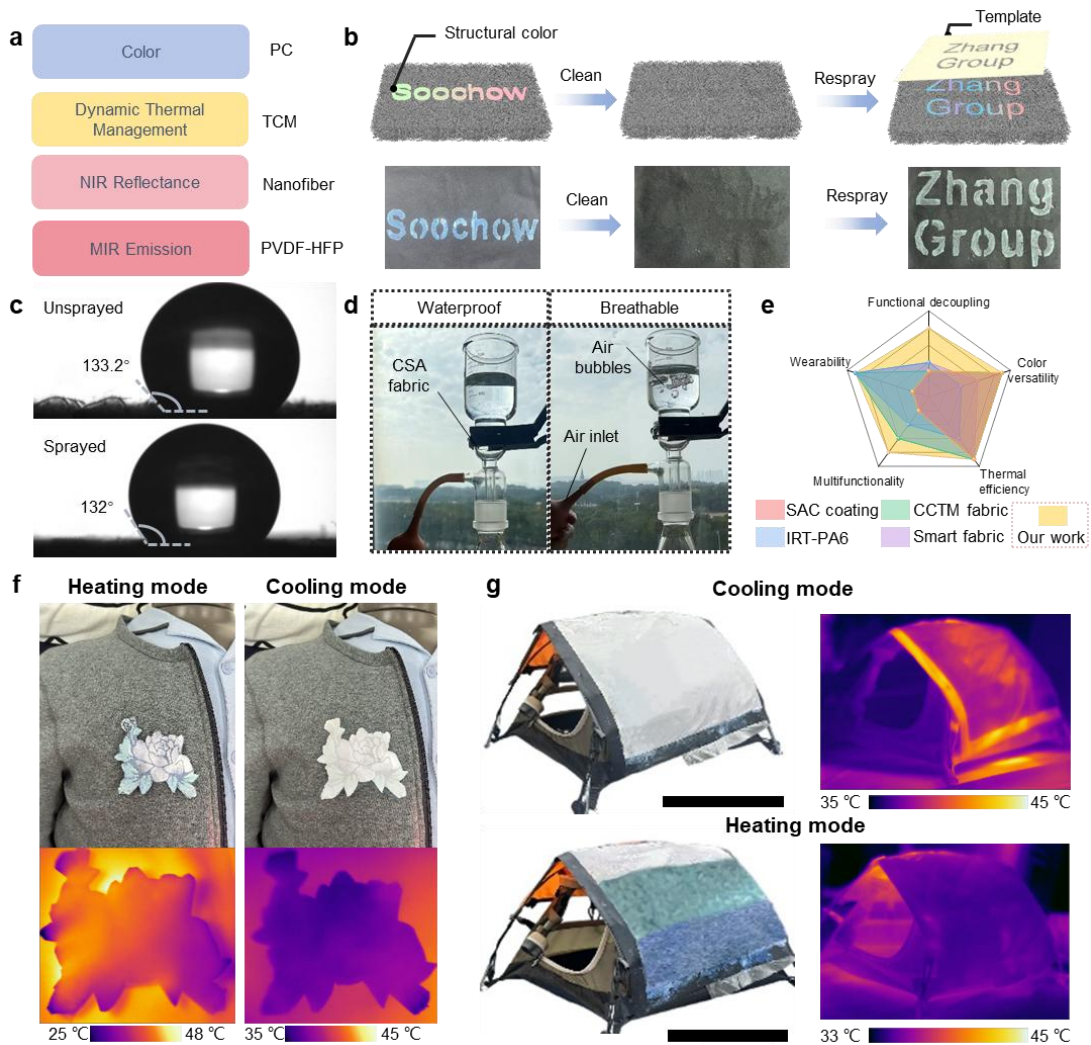


Fig. 5 Application performance and multifunctional advantages of CSA fabric. a) Modular design of CSA fabric. b) Color-rewritable behavior of CSA fabric. c) WCA of CSA fabric. d) Waterproofing and air permeability of CSA fabric. e) Radar plot comparing CSA fabric with existing radiation-modulating materials^{13-15,32}. f) Wearable prototype (flower-patterned CSA fabric on garment) with thermal images. g) Intelligent tent prototype maintaining stable internal microenvironment (Scale bar: 10 cm).

Supplementary Information

Thermally adaptive textile inspired by morpho butterfly for all-season comfort and visible aesthetics

Zhuowen Xie^{1#}, Yan Wang^{1#}, Ting-Ting Li¹, Wangkai Jiang^{1}, Honglei Cai¹, Jun Zhang¹, Hui Wang¹, Jianchen Hu^{1*}, Ke-Qin Zhang^{1*}*

¹ National Engineering Laboratory for Modern Silk, College of Textile and Clothing Engineering, Soochow University, Suzhou, Jiangsu 215123, China

These authors contributed equally: Zhuowen Xie, Yan Wang. Correspondence and requests for materials should be addressed to W. J. (wangkaijiang279@gmail.com), J. H. (hujianchen@suda.edu.cn) or K.-Q. Zhang (kqzhang@suda.edu.cn).

Experimental details

Materials

N,N-dimethylformamide (DMF), acetone (AC), and poly(vinylidene fluoride-co-hexafluoropropylene) (PVDF-HFP) were purchased from Shanghai Aladdin Biochemical Technology Co., Ltd. Styrene (St, analytical reagent (AR) grade), potassium persulfate (KPS, AR grade), and sodium dodecyl sulfate (SDS, AR grade) were obtained from Sinopharm Chemical Reagent Co., Ltd. Thermochromic microcapsules (TCMs), with a critical thermochromic phase transition temperature of approximately 25 °C, were purchased from Shenzhen Fantasy Chromic Technology Co., Ltd.

Supplementary Note 1: Methods

Fabrication of SA fabric

SA fabric was fabricated through electrospinning. Specifically, PVDF-HFP (20 wt%) was dissolved in a mixed solvent of AC (30 vol%) and DMF (70 vol%). The mixture was heated and stirred for 2 hours to form a uniform organic dispersion. Subsequently, black-white TCMs (10 wt%) were dispersed into the dispersion and stirred for 30 minutes to obtain the electrospinning precursor solution. The solution was then used for SA fabric preparation *via* electrospinning.

The electrospinning parameters were as follows: a 23-gauge spinning needle, applied voltage of 12 kV, feed rate of 1 mL h⁻¹, and needle reciprocation speed of 5 cm min⁻¹ (maintained perpendicular to the electric field). A collector (aluminum foil wrapped with silicone oil paper) was positioned 10 cm from the needle tip. Electrospinning was performed at an ambient temperature of 25±2 °C and humidity of 35±5%.

Fabrication of CSA fabric

CSA fabric was fabricated by spraying a polystyrene (PS) nanoparticle layer onto SA fabric (substrate). The preparation process comprised two main stages: synthesis of

PS nanospheres via emulsion polymerization, and subsequent spraying of size-tuned PS dispersions for structural color display.

Stage 1: Synthesis of PS nanospheres via emulsion polymerization

First, a specific amount of St (14-25 mL) and 80 mL of pure water (initial solution) were added to a flask, which was then placed in a water bath. The water bath was heated to a target temperature of 85 °C with stirring at 650 rpm. Next, 0.45 g of KPS and 0.015 g of SDS were dissolved in 20 mL of pure water to prepare a suspension. After the water bath reached 85 °C and stabilized for 3–5 minutes, the SDS suspension was added to the flask. The mixture was stirred at 85 °C under sealed conditions for 6 hours, ultimately yielding PS nanospheres with tunable particle sizes. A 10 wt% aqueous dispersion of the PS nanospheres was prepared for subsequent use.

Stage 2: Spraying for structural color display

To achieve distinct structural colors in the CSA fabric, PS nanosphere dispersions with different particle sizes were sequentially sprayed onto the SA fabric substrate. This step ensured the final fabric exhibited the desired variations in bright, angle-independent structural colors.

Characterization

The morphologies of the SA fabric and CSA fabric were characterized by scanning electron microscopy (SEM, Hitachi S8100). FTIR spectroscopy (Bruker Vertex 70) was used to analyze the chemical composition of the SA fabric, confirming abundant absorption peaks in the atmospheric transparency window. Thermal images were captured by an infrared thermal camera (FORTIC 226) to visualize temperature distribution.

Optical characterization of samples

The optical properties of the textiles (including CSA and SA fabrics) were characterized across different spectral ranges. For the ultraviolet-visible-near-infrared (UV-VIS-NIR, 0.3–2.5 μm) range, reflectance (ρ) spectra were measured using a UV-3600 Plus spectrometer (Shimadzu, Japan) equipped with a gold-coated integrating

sphere. For the mid-infrared (MIR, 2.5–25 μm) range, ρ spectra were acquired *via* a Fourier transform infrared (FTIR) spectrometer (Nicolet iS50, Thermo Fisher Scientific, USA) combined with a gold integrating sphere (PIKE Technologies, USA). Absorptance (α) and emissivity (ε) spectra were derived from the relation $\alpha=\varepsilon=1-\rho-\tau$ (Kirchhoff's law), assuming negligible transmittance ($\tau\approx0$) for opaque textiles.

Additionally, the visible reflectance of polystyrene (PS) nanoparticles (380–760 nm) was measured using a UV-2000DH spectrometer (Shanghai Fuxiang Co., Ltd., China). For thermal infrared characterization (2.5–25 μm), reflectance signals were collected with an FTIR spectrometer (Nicolet 6700, Thermo Fisher Scientific, USA) equipped with a gold integrating sphere.

Wetting State Characterization

Prior to SEM characterization, the samples were sputter-coated with a thin platinum layer to enhance conductivity. Energy dispersive spectroscopy (EDS) was employed to map the elemental distribution within the samples. ImageJ software was used for image processing, including statistical analysis of the sizes and distributions of TCMs, PVDF-HFP nanofibers, and PS nanospheres, as well as quantification of the fabric microstructure and cross-sectional thickness.

Surface wetting properties were evaluated as follows: A 5 μL droplet of deionized water was deposited on the fabric surface, and the static contact angle was measured using a video optical contact angle system (OCA 20, DataPhysics Instruments, Germany). Five random points were selected on each fabric surface, and the average contact angle was calculated to ensure reproducibility.

Definitions of solar reflectance and thermal emittance

The average reflectance ($\bar{\rho}_{\text{solar}}$) of the ultraviolet to near infrared light (0.25–2.5 μm) was obtained by Eq. S1¹.

$$\bar{\rho}_{\text{solar}} = \frac{\int_{0.25 \mu\text{m}}^{2.5 \mu\text{m}} I_{\text{solar}}(\lambda) R_{\text{solar}}(\lambda) d\lambda}{\int_{0.25 \mu\text{m}}^{2.5 \mu\text{m}} I_{\text{solar}}(\lambda) d\lambda} \quad (\text{S1})$$

where λ is the wavelength, $I_{\text{solar}}(\lambda)$ is the normalized ASTM G173 Global solar

intensity spectrum, and $R_{solar}(\lambda)$ is surface spectral reflectance of samples.

The average infrared thermal emittance ($\bar{\varepsilon}_{ASTW}$) in the atmospheric transmittance window (8-13 μm) is defined as²:

$$\bar{\varepsilon}_{ASTW} = \frac{\int_{8 \mu\text{m}}^{13 \mu\text{m}} I_{BB}(T, \lambda) \varepsilon_{ASTW}(\lambda) d\lambda}{\int_{8 \mu\text{m}}^{13 \mu\text{m}} I_{BB}(T, \lambda) d\lambda} \quad (\text{S2})$$

where $I_{BB}(T, \lambda)$ is the blackbody radiation intensity at a temperature of T calculated by Planck's law³:

$$I_{BB}(T, \lambda) = \frac{2hc^2}{\lambda^5} \frac{1}{e^{\frac{hc}{\lambda T k_B}} - 1} \quad (\text{S3})$$

where h is the Planck constant, c is the speed of light in a vacuum, k_B is the Boltzmann constant. In the present work, the temperature T is set as 298 K.

Thermal management output measurement

The thermal management performances of SA and CSA fabric were evaluated using a custom-built experimental setup. A xenon lamp equipped with an AM 1.5 filter served as a solar simulator to provide controllable solar irradiance (0–1000 $\text{W}\cdot\text{m}^{-2}$, adjustable intensity). Thermal infrared images were captured using an infrared thermal imager to visualize the fabric's surface temperature distribution during testing.

Supplementary Note 2: Scattering efficiency calculation

The scattering efficiency (Q_{sca}) of PVDF-HFP nanofibers in the SA fabric was calculated based on Mie scattering theory, which describes electromagnetic wave scattering by spherical particles (here, approximated as cylindrical fibers with equivalent scattering cross-sections). The calculation was implemented *via* a custom script in MATLAB R2021a, incorporating the following parameters:

Fiber geometry: Diameter range of 0.3–1.3 μm , matching the experimentally observed distribution of electrospun PVDF-HFP nanofibers.

Refractive indices (n): PVDF-HFP nanofibers: $n_{\text{fiber}}=1.40$ (typical value for PVDF-HFP copolymers in the visible-near-infrared spectrum); Surrounding medium (air): $n_{\text{medium}}=1.00$.

Incident light: Solar spectrum range (0.3–2.5 μm), divided into visible (VIS, 0.4–0.75 μm) and near-infrared (NIR, 0.75–2.5 μm) sub-ranges for targeted analysis.

The MATLAB script computed Q_{sca} as a function of fiber diameter (d) and wavelength (λ), solving the Mie equations for cylindrical geometries. Key outputs included: Q_{sca} versus d curves, showing peak scattering efficiency.

Supplementary Note 3: Theoretical thermal calculation of thermal emitter

We used a traditional simple model to analyze the energy balance of the thermal emitter, with several parts to the radiation: the emitted thermal radiation from the thermal emitter (P_{rad}), the absorbed thermal radiation from the atmosphere (P_{atm}), the heat transfer by thermal conduction and thermal convention ($P_{cond+conv}$) and the absorbed thermal radiation from sunlight (P_{solar}). The energy balance equation is as follows⁴⁻⁷:

$$P_{cooling}(T, T_{amb}) = P_{rad}(T) - P_{atm}(T_{amb}) - P_{solar} - P_{cond+conv} \quad (\text{S4})$$

where T is the surface temperature of the EM-textiles and T_{amb} is the ambient temperature. $P_{rad}(T)$ is the thermal power radiated by the EM-textiles, $P_{atm}(T_{amb})$ is the absorbed atmospheric thermal radiation at T_{amb} . P_{solar} is the incident solar irradiation absorbed by the EM-textiles, and $P_{cond+conv}$ is the power lost due to convection and conduction. The net cooling power defined in Eq. (S4) can reach a high value by increasing the radiative power of the EM-textiles and reducing either the solar absorption or parasitic heat gain. These parameters can be calculated by the following equations:

$$P_{rad}(T) = A \int d\Omega \cos\theta \int_0^{\infty} d\lambda I_{BB}(T, \lambda) \varepsilon(\lambda, \theta) \quad (\text{S5})$$

$$P_{atm}(T_{amb}) = A \int d\Omega \cos\theta \int_0^{\infty} d\lambda I_{BB}(T_{amb}, \lambda) \varepsilon(\lambda, \theta) \varepsilon_{atm}(\lambda, \theta) \quad (\text{S6})$$

$$P_{solar} = A \int_0^{\infty} d\lambda \varepsilon(\lambda, \theta_{solar}) I_{AM1.5}(\lambda) \quad (\text{S7})$$

$$P_{cond+conv} = Ah_c(T_{amb} - T) \quad (\text{S8})$$

where A is the surface area of the EM-textiles. $\int d\Omega = 2\pi \int_0^{\pi/2} d\theta \sin\theta$ is the angular integral over a hemisphere. The variable θ denotes the zenith angle, which is

the angle between the direction of radiation and the surface normal. $\varepsilon(\lambda, \theta)$ is the directional emissivity of the surface at wavelength λ . $\varepsilon_{atm}(\lambda, \theta)=I-\tau(\lambda)^{\lambda/\cos\theta}$ is the angle-dependent emissivity of the atmosphere; $\tau(\lambda)$ is the atmospheric transmittance in the zenith direction. $P_{rad}(T)$ and $P_{atm}(T_{amb})$ are determined by both the spectral data of the EM-textiles and the emissivity spectrum of the atmosphere according to MODTRAN of Mid-Latitude Summer Atmosphere Model⁷. In Eq. (S7), the solar irradiance is represented by the AM1.5 spectrum ($I_{AM1.5}(\lambda)$). In Eq. (S8), $h_c=h_{cond}+h_{conv}$ is a combined nonradiative heat coefficient that captures the collective effect of conductive and convective heating, which can be limited to a range between 0 and 12 W m⁻² K⁻¹.

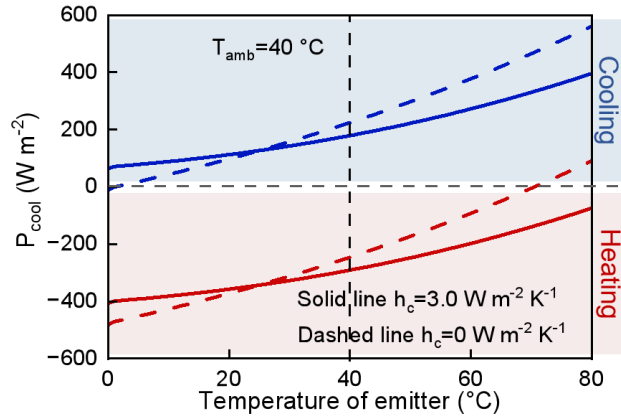


Fig. S1 Cooling power of an emitter as a function of its temperature at different heat transfer coefficients ($T_{\text{amb}}=40\text{ }^{\circ}\text{C}$).

Steady-state radiative-convective model calculating cooling power (P_{cool}) of the emitter (CSA fabric analog). Two scenarios: VIS reflective (cooling state, $\rho_{\text{solar}}\approx 1$) yields positive P_{cool} (net heat dissipation), VIS absorptive (heating state, $\rho_{\text{solar}}\approx 0.5$) yields negative P_{cool} (passive heating). Validates bidirectional thermal regulation *via* VIS light management (aligns with Fig. 1d). Additionally, the h simulates different environmental convection conditions to quantify the textile's adaptability in practical applications.

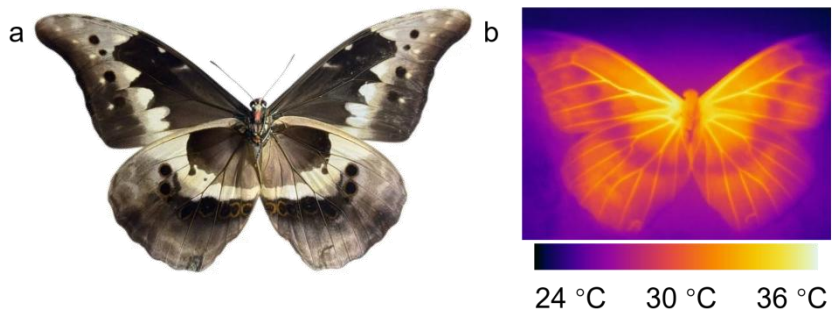


Fig. S2 Digital photos and infrared thermal images of the dorsal side of a morpho butterfly under xenon lamp irradiation ($600 \text{ W}\cdot\text{m}^{-2}$).

The natural decoupling of structural color and thermal performance. Infrared thermal images reveal significant temperature variations: black substrates (absorbing more solar energy) exhibit higher temperatures than white substrates, despite identical structural coloration. This phenomenon inspired the bio-inspired layered textile design, separating structural color (PCs) and thermochromic functions (TCMs) for independent thermal regulation. Temperature distribution was captured *via* a high-resolution infrared camera (FOTRIC 226s), validating the feasibility of decoupled color-thermal control.

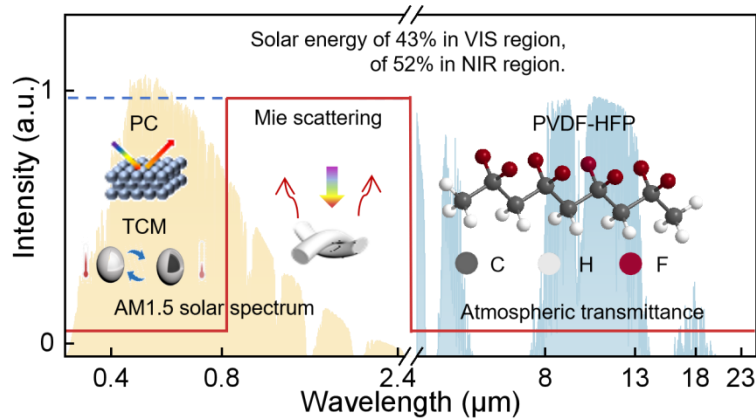


Fig. S3 Design and interaction of functional materials with the solar spectrum and atmospheric window.

Illustration of the optical design of CSA fabric, highlighting its interaction with the solar spectrum (0.25–2.5 μm) and atmospheric transparency window (8–13 μm). Based on the optical switching mechanism, the fabric exhibits bidirectional thermal regulation:

Cooling mode: High solar reflectance ($\rho_{\text{solar}} \approx 0.9$) and high mid-infrared emissivity ($\varepsilon_{\text{MIR}} \approx 0.94$) for radiative heat dissipation;

Heating mode: High solar absorptance ($\alpha_{\text{solar}} \approx 0.5$) for passive solar heating.

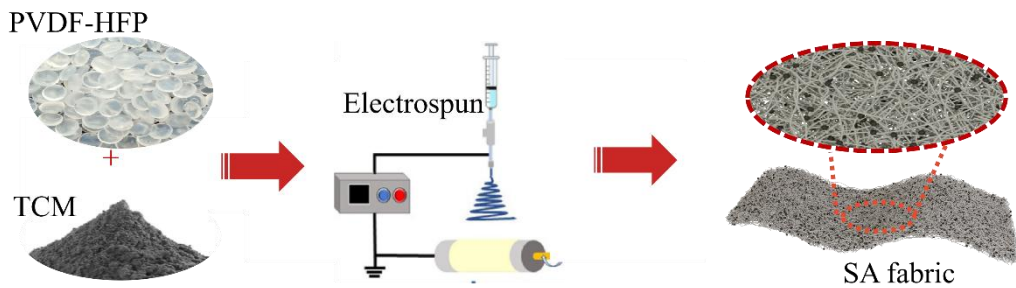


Fig. S4 Fabrication of the thermochromic SA fabric: electrospinning of the functional PVDF-HFP/TCM composite nanofibers.

The fabrication process of the thermochromic SA fabric is through electrospinning of PVDF-HFP and TCM composite nanofibers. Experimental parameters include a voltage of 12 kV, flow rate of 1 mL/h, and needle-to-collector distance of 10 cm, under controlled conditions ($25 \pm 2^\circ\text{C}$, $35 \pm 5\%$ humidity). This process ensures uniform TCM distribution, enabling reversible optical switching (black state for heating, white state for cooling).

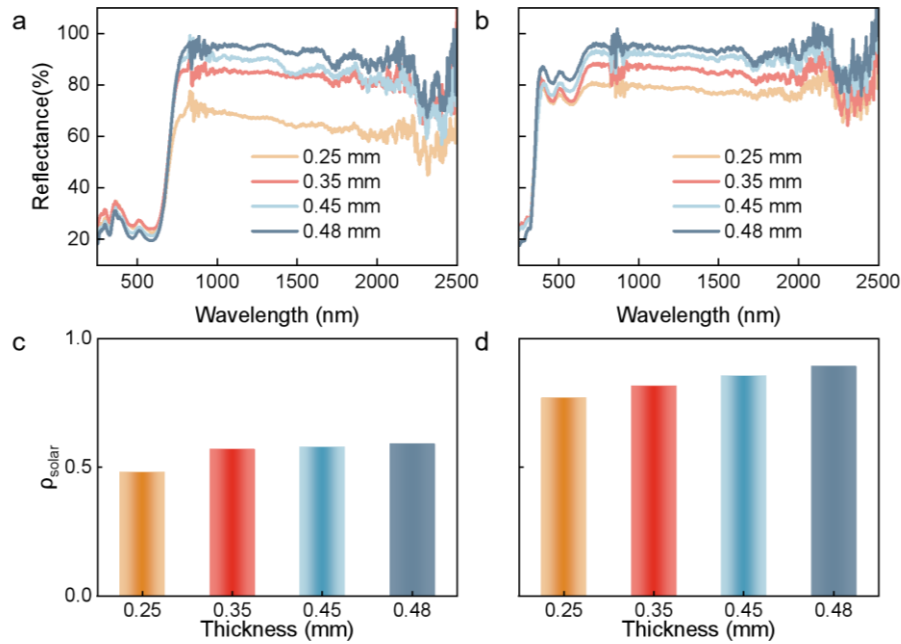


Fig. S5 (a) Comparison of reflectance spectra under different mode and thicknesses, covering the UV-VIS-NIR range (0.25–2.5 μ m). (b) Thickness and its impact on ρ_{solar} . Comparison of SA fabric reflectance spectra and ρ_{solar} at $T < 25$ °C (heating mode) and $T > 25$ °C (cooling mode). Low T shows $\rho_{VIS} \approx 20\%$ (enhanced absorption), high T shows $\rho_{VIS} \approx 80\%$ (enhanced reflectance), confirming thermochromic switching. Measured by UV-VIS-NIR spectrometer (UV-3600, Shimadzu), guiding thickness optimization.

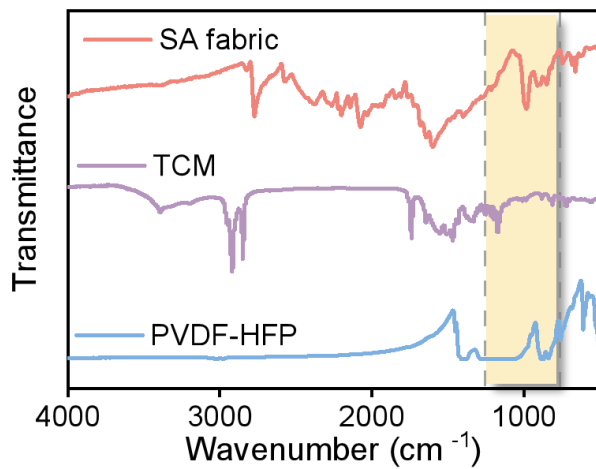


Fig. S6 FTIR transmittance spectra of SA fabric, TCM, and PVDF-HFP.

The FTIR transmittance spectra of SA fabric, TCM, and PVDF-HFP across the mid-infrared range (2.5-20 μm). Experiments used an FTIR spectrometer (Nicolet IS50) with a gold integrating sphere; samples were prepared as thin films. Characteristic peaks, such as C-F vibrations ($\sim 1100 \text{ cm}^{-1}$) for PVDF-HFP and functional groups for TCM, are labeled to verify chemical integrity.

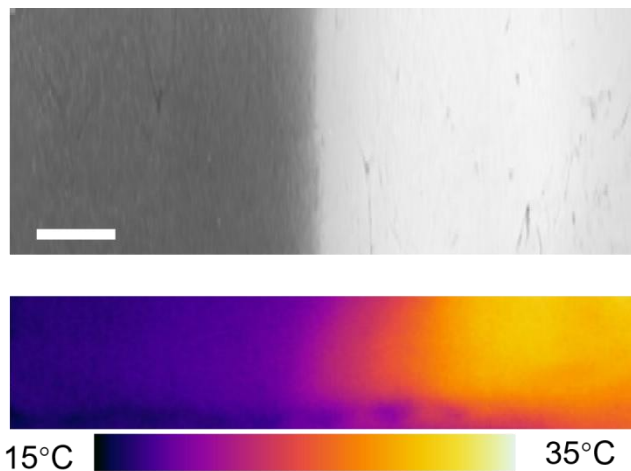


Fig. S7 Optical and thermal images of the solar irradiation experiment setup (scale bar: 2 cm).

A thermal camera (FOTRIC 226) recorded real-time temperatures, validating the adaptive performance of the SA fabric under simulated solar flux ($0\text{-}1000\text{ W m}^{-2}$): heating at low temperatures and cooling at high temperatures. Results align with indoor experiments in Section 2.1, demonstrating temperature-triggered switching.

The solar irradiation experiment setup is using a xenon lamp simulator with an AM 1.5 filter, showing a surface temperature gradient from $\sim 15\text{ }^{\circ}\text{C}$ to $\sim 35\text{ }^{\circ}\text{C}$. The setup includes an insulated chamber with an aluminum foil coating to minimize parasitic heat exchange.

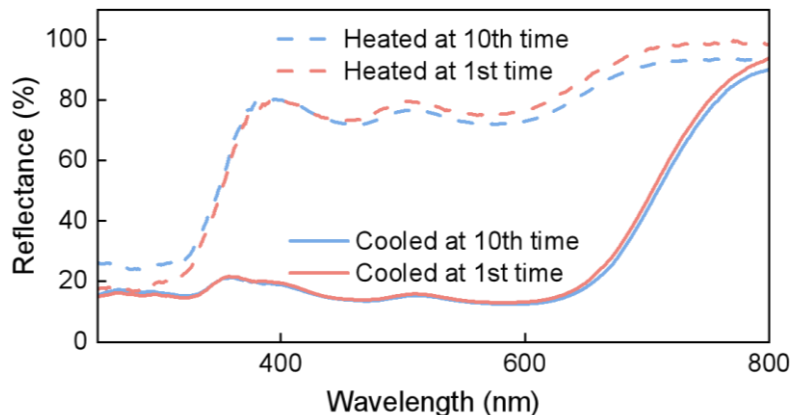


Fig. S8 Reflectance spectra of the SA fabric after the 1st and 10th heating-cooling cycles.

The reflectance spectra of SA fabric after the 1st and 10th heating-cooling cycles (15-40 °C), are assessing the robustness of optical switching. Cyclic tests show less than 5% variation in reflectance, confirming the reversible stability of TCMs. Experiments used a spectrometer in the visible range (0.4-0.75 μm), with each cycle involving heating to 40 °C and cooling to 15 °C.

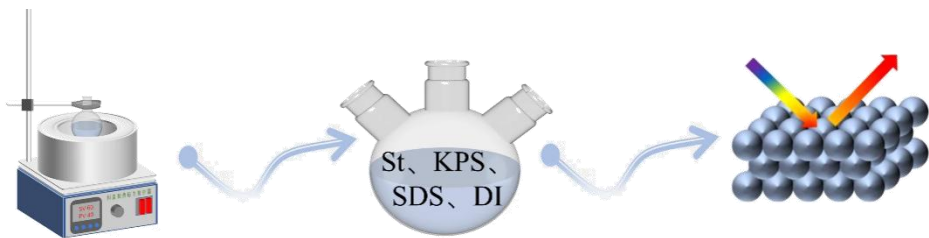


Fig. S9 Fabrication of PS nanoparticles.

The fabrication of PS nanoparticles via emulsion polymerization for the structural color layer of CSA fabric. Experimental parameters include St volumes of 14-25 mL, KPS, and SDS, stirred at 85°C for 6 hours. The resulting PS nanospheres (diameters 180-240 nm) produce Bragg reflection-based structural colors. This method ensures monodispersity, providing a foundation for spray coating.

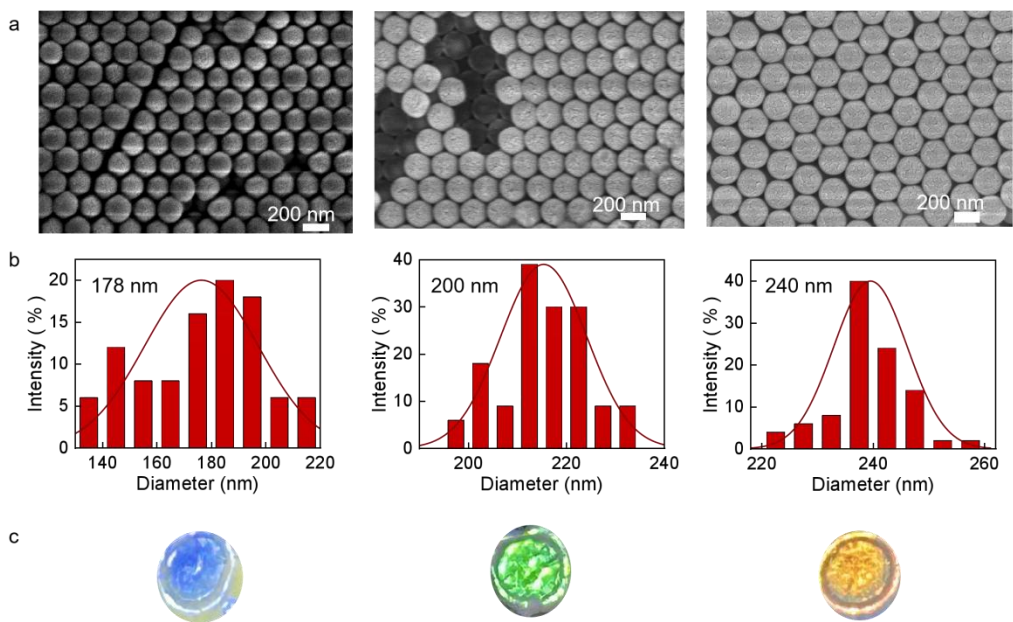


Fig. S10 SEM images and size distribution histograms of PS nanospheres with diameters of 178, 200, and 240 nm.

SEM images and size distribution histograms of PS nanospheres with target diameters of 178, 200, and 240 nm. SEM reveals high monodispersity (average diameters \sim 180 nm, \sim 220 nm, \sim 240 nm), with statistically analyzed using ImageJ software. These nanospheres enable structural color tuning, as diameter dictates the Bragg reflection wavelength. Experiments used SEM (Regulus 8100) for characterization, guiding color customization in CSA fabrics.

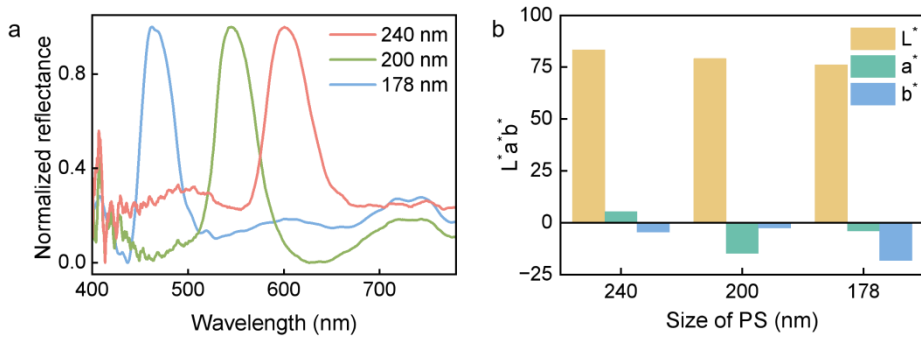


Fig. S11 Reflectivity spectra and L*a*b*coordinates of PS nanospheres with varying diameters (178, 200, 240 nm).

This figure shows the reflectance spectra and CIE L*a*b* color coordinates of PS nanospheres with diameters of 178, 200, and 240 nm, covering the visible range (380-760 nm). Reflectance spectra exhibit distinct peaks (e.g., 240 nm nanospheres correspond to red reflection), and L*a*b* coordinates confirm high saturation. Experiments used a spectrometer (200-DH), with color coordinates based on the CIE 1931 standard. Results validate the tunability of structural colors, consistent with the spectral analysis.

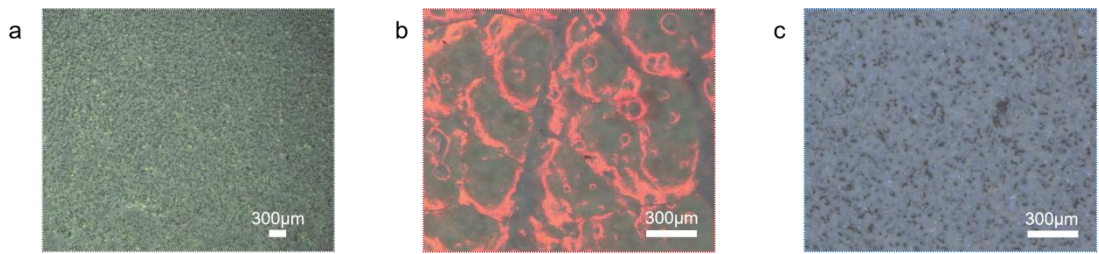


Figure S12. Optical micrographs of PS nanospheres with varying diameters (178, 200, 240 nm).

Optical micrographs of PS nanospheres with diameters of 178, 200, and 240 nm, visually demonstrating their structural color effects. Images, captured under visible light microscopy, show vibrant, uniform colors. Experiments combined SEM data to verify confined assembly within micropores, minimizing defects. This method underpins the visual aesthetics of the textile.

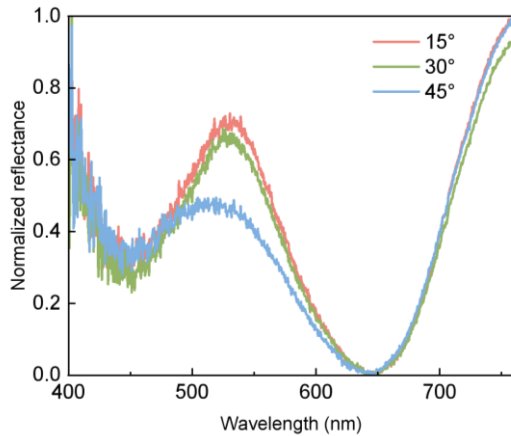


Fig. S13 Angle-insensitive optical performance of green CSA fabrics.

The normalized reflectance spectra of the green CSA fabric measured at three distinct observation angles: 15°, 30°, and 45°, spanning the VIS wavelength range. The three spectral curves exhibit remarkable overlap across the entire spectral region, with particularly close alignment in the 500-700 nm range. The observed angle-independent behavior is a characteristic signature of the structural color layer integrated into the CSA fabric, which maintains consistent chromaticity and reflectance regardless of the observer's position.

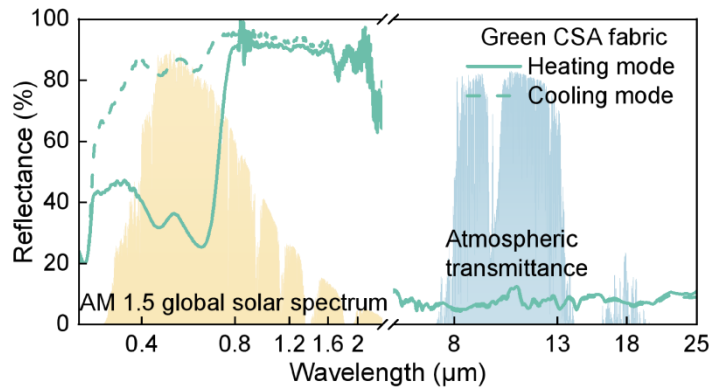


Fig. S14 Spectral reflectance of the green CSA fabric in cold and hot states, benchmarked against the AM 1.5 global solar spectrum and atmospheric transmittance.

Solar reflectance switch from ~ 0.5 (heating state) to ~ 0.9 (cooling state), with a difference exceeding 30% (Section 2.2). Emissivity in the atmospheric window (8-13 μm) remains stable ($\varepsilon \approx 0.94$). Experiments used UV-VIS-NIR spectrometers, validating bidirectional optical regulation.

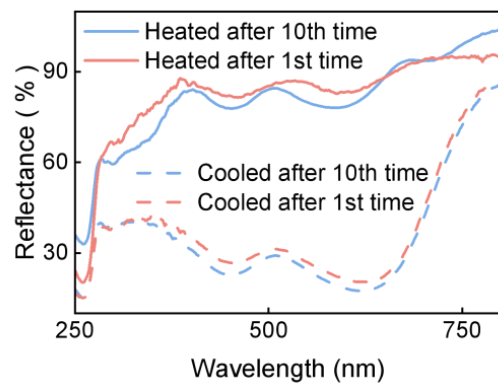


Fig. S15 Reflectance spectra of the green CSA fabric after the 1st and 10th heating-cooling cycles.

The reflectance spectra of green CSA fabric after the 1st and 10th heating-cooling cycles (15-40 °C), evaluate the durability of the structural color layer. Post-cycling spectra show negligible changes, confirming the stability of PS nanospheres under thermal switching.



Fig. S16 A CSA fabric sprayed on PS nanoparticles, using a flower model template.

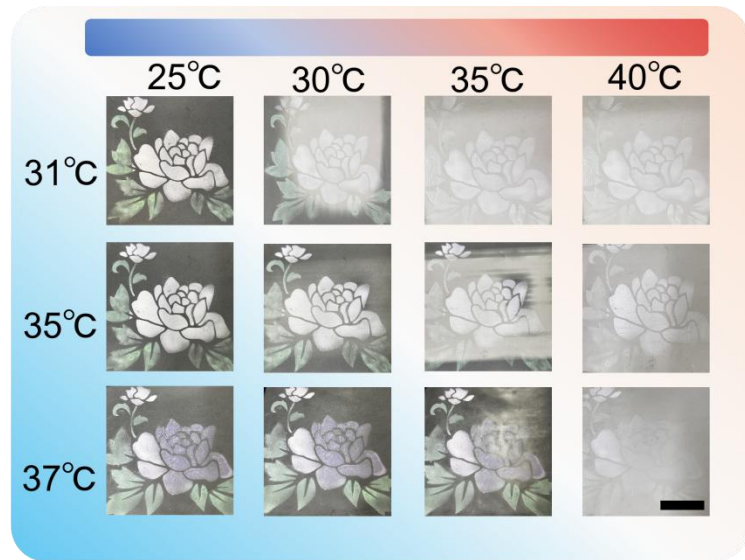


Fig. S17 Visual characterization: response of a floral pattern sprayed on a CSA fabric of T_c (31, 35, 37 °C) and T_{amb} (25, 30, 35, 40 °C) temperatures.

This figure presents the visual response of a floral pattern on the CSA fabric across critical temperatures ($T_c=31, 35, 37$ °C) and ambient temperatures (25, 30, 35, 40 °C). It systematically quantifies thermochromic behavior, highlighting T_c tunability.

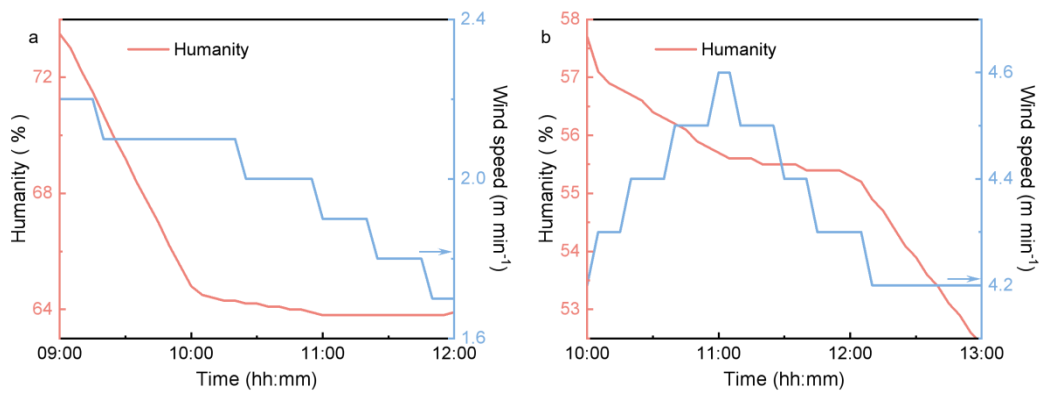


Fig. S18 Environmental humidity and wind speed monitoring during outdoor thermal tests under a) hot and b) cold conditions.

We adopted the local solar power data obtained from the Solcast API Toolkit (39), which is consistent with our pyranometer irradiance characterizations.

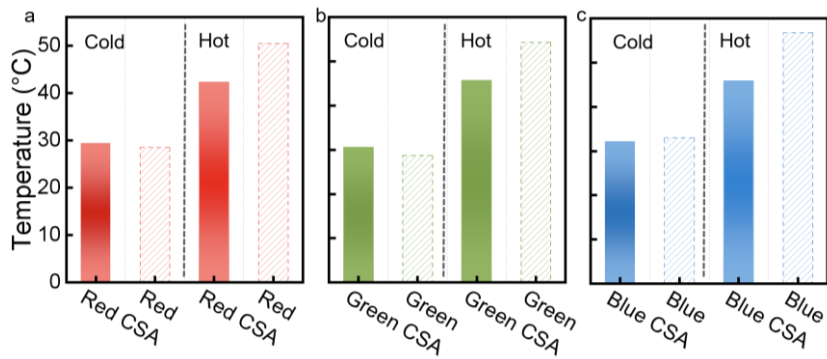


Fig. S19 Quantitative outdoor performance comparison of CSA fabrics: a) Red, b) Green, and c) Blue with commercial-colored fabrics across seasons.

In the cold environment, the CSA fabrics consistently demonstrate a significantly higher steady-state temperature than the commercial fabrics of the same apparent color. The measured temperature differentials are approximately 5 °C for red, 7 °C for green, and 8 °C for blue, indicating the superior passive heating capability of the CSA design. Conversely, in the hot environment, the CSA fabrics exhibit a significantly lower steady-state temperature compared to the commercial fabrics. The cooling differentials are similarly pronounced, at approximately 5 °C for red, 6 °C for green, and 7 °C for blue.

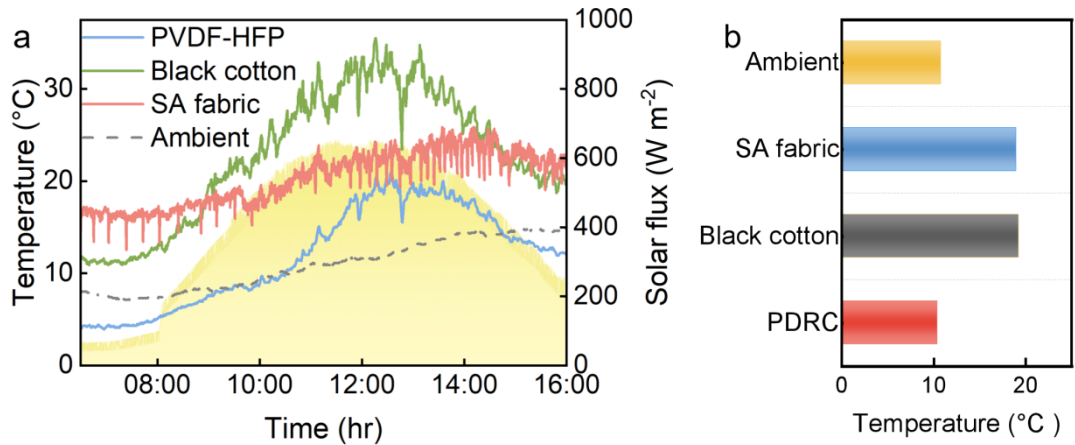


Fig. S20 Comparative thermal performance under solar irradiation: a) Time-dependent surface temperature profiles of SA fabric, black cotton, PVDF-HFP, and ambient air, offering a body temperature ($\sim 34^{\circ}\text{C}$), alongside concurrent solar flux; b) Statistical comparison of the average temperatures for each material and ambient.

Compares the thermal performance of SA fabric, black cotton, PVDF-HFP, and ambient air: (a) time and solar irradiation-dependent surface temperature profiles, showing SA fabric's smart adaptive thermal management; (b) statistical average temperatures. Experiments used a thermocouples and a itech DC power supply (IT6832) offered a body temperature under ambient conditions. Results validate the adaptive performance of SA fabric, aligning with Fig. 2h and highlighting its superiority over conventional materials.

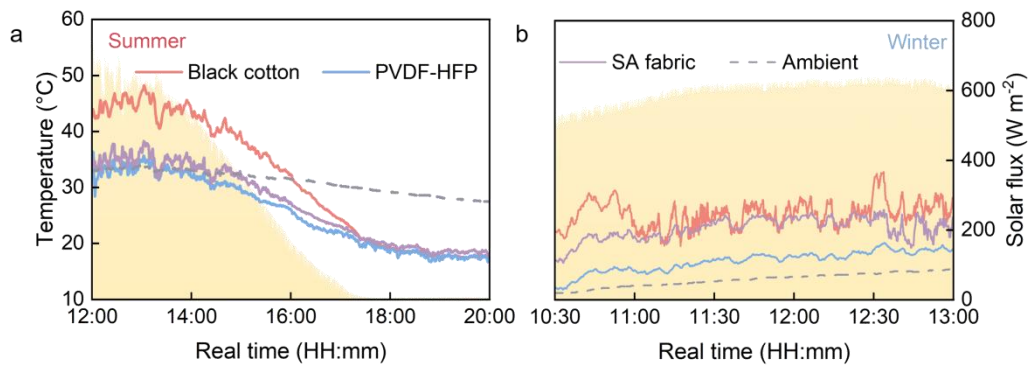


Fig. S21 Dual-season comparison of thermal behavior for different materials under different season (a) Summer. b) Winter)

Compares the dual-season (cold / hot) thermal behavior of different materials under varying solar flux, showing the CSA fabric's heating mode in cold conditions (e.g., 15 °C) and cooling mode in hot conditions (e.g., 35 °C). Experiments integrated outdoor data (Section 2.3) with meteorological recordings of solar flux and ambient parameters. Results emphasize the textile's advantage in climate adaptation.

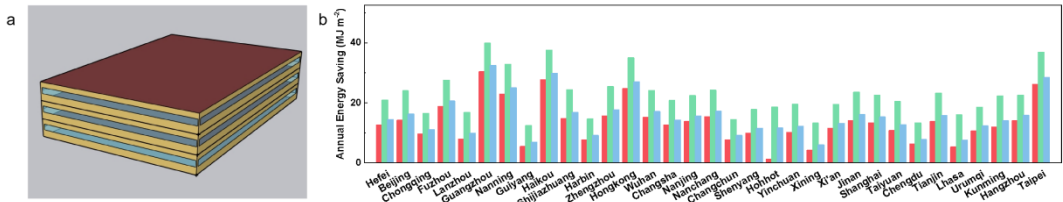


Fig. S22 a) Model in EnergyPlus. b) Comparative analysis of simulated annual energy saving potential across major Chinese cities.

The results of a nationwide simulation study, quantifying the annual energy saving potential per unit area (MJ m^{-2}) for selected cities across China. The X-axis lists 29 major cities, geographically spanning from the cold northern regions (e.g., Harbin) to the hot southern zones (e.g., Haikou), including key municipalities like Beijing, Shanghai, and Taipei. The Y-axis measures the simulated energy savings, ranging from 0 to 40 MJ m^{-2} .

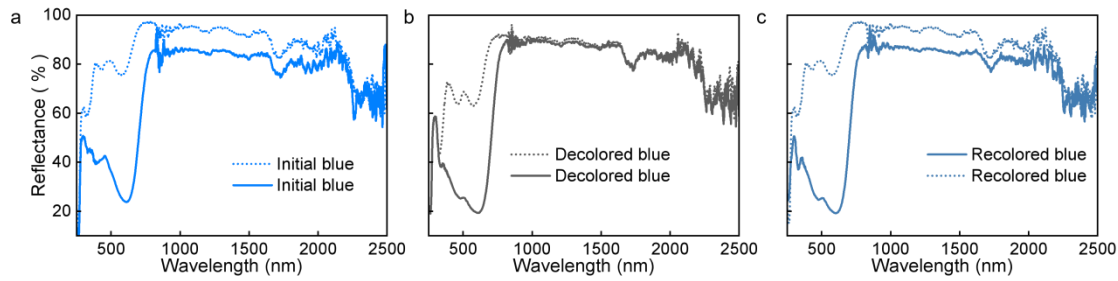


Fig. S23 Reflectance spectra of the blue CSA fabric in three treatments: a) initial, b) decolored, and c) recolored at different states (dashed line: cooling state, solid line: heating state).

The reflectance spectra of blue CSA fabric in initial, decolored (after washing), and recolored states at cooling / heating state.. Spectra confirm that color respray does not compromise optical performance, with reflectance differences remaining stable. Experiments involved wash-respray cycles, with results consistent with durability tests, supporting multifunctional applications.

References

- 1 Li, D. *et al.* Scalable and hierarchically designed polymer film as a selective thermal emitter for high-performance all-day radiative cooling. *Nat. Nanotechnol.* **16**, 153-158 (2021).
- 2 Zeng, S. *et al.* Hierarchical-morphology metafabric for scalable passive daytime radiative cooling. *Science* **373**, 692-696 (2021).
- 3 Lei, Z., Gao, W. & Wu, P. J. Double-network thermocells with extraordinary toughness and boosted power density for continuous heat harvesting. *Joule* **5**, 2211-2222 (2021).
- 4 Zhu, B. *et al.* Subambient daytime radiative cooling textile based on nanoprocessed silk. *NATURE NANOTECHNOLOGY* **16**, 1342-U1336, doi:10.1038/s41565-021-00987-0 (2021).
- 5 Song, J. N. *et al.* Durable radiative cooling against environmental aging. *NATURE COMMUNICATIONS* **13**, doi:10.1038/s41467-022-32409-7 (2022).
- 6 Fan, S. H. & Li, W. Photonics and thermodynamics concepts in radiative cooling. *NATURE PHOTONICS* **16**, 182-190, doi:10.1038/s41566-021-00921-9 (2022).
- 7 Wang, T. *et al.* A structural polymer for highly efficient all-day passive radiative cooling. *NATURE COMMUNICATIONS* **12**, doi:10.1038/s41467-020-20646-7 (2021).